

# Pinning Disfavors Nucleation in Colloidal Vapor Deposition

Noman Hanif Barbhuiya<sup>1†</sup>, Pritam K. Mohanty<sup>1†</sup>, Saikat Mondal<sup>2</sup>, Aminul Hussian<sup>1</sup>,  
Adhip Agarwala<sup>2</sup>, Chandan K. Mishra<sup>1\*</sup>

<sup>1</sup>Department of Physics, Indian Institute of Technology Gandhinagar, Palaj, Gandhinagar, 382055, Gujarat, India

<sup>2</sup>Department of Physics, Indian Institute of Technology Kanpur, Kalyanpur, Kanpur, 208016, Uttar Pradesh, India

<sup>†</sup>These authors contributed equally to this work

\*To whom correspondence should be addressed; E-mail: chandan.mishra@iitgn.ac.in

**Vapor deposition, known for precise structural control, is inevitably influenced by impurities. These impurities, often distinct from the depositing material, can significantly impact material properties, including local structure. Interestingly, the effect of immobilizing some of the depositing particles themselves, which would still preserve local structural symmetry, remains largely unexplored. By introducing a small fraction of pinned sites during colloidal vapor deposition and employing a combination of thermodynamic and kinematic measurements, we demonstrate that pinned sites, termed as "mobility impurities," are disfavored as nucleation centers. Moreover, tuning the mobility of mobile colloids can adjust nucleation likelihood. In later stages of growth, pinning induces mode localization, altering the thin film's vibrational spectrum. Our research thus underscores the potential of strategically incorporating mobility impurities to engineer material properties.**

## Introduction

The introduction of impurities, whether intentional or otherwise, during the initial stages of material fabrication holds considerable sway over a spectrum of material properties and their ensuing performance, such as structure (1–3), mechanical strength (4–6) and transport properties (7, 8). These impurities, often extrinsic, differ from the primary constituents of the material in terms of one or more physical and chemical attributes and exert their

influence by modifying the free energy landscape, thereby altering nucleation and growth of the materials (9–13). For example, in processes akin to vapor deposition, the presence of impurities can lead to diverse outcomes: they might lower the interfacial barriers to crystallization (9), and promote smoother film formation with reduced defect density (14, 15), regulate the rate of nucleation and the morphology of growing islands (1), or impede crystal growth altogether (12, 16).

Modifications to free energy landscape in the presence of impurities can arise due to their contrasting pair potentials (3, 17), shape and size (9, 18), and/or diffusion barriers (11, 19) with the depositing particles, often modifying structural properties of the materials. However, the potential impact of immobilizing some of the depositing particles themselves on the substrate during the initial stages of film growth, in which case the immobilized particle’s interaction with mobile particles is identical to the interaction between any two mobile particles, remains largely unexplored (20). Immobilized depositing particles, which we will refer to as "mobility impurities," are differentiated from freely diffusing counterparts solely by their diffusion barriers resulting from their interactions with the substrate. Notably, mobility impurities would still preserve any structural correlations.

To address this gap, we pinned a small fraction of parent colloidal particles to the substrate in colloidal vapor deposition experiments, serving as our desired mobility impurities. Employing video microscopy, we observed the spatiotemporal evolution of clusters, encompassing their formation, evolution, disintegration, and growth at a single-particle level, both with and without pinned particles. Our experiments reveal distinct thermodynamic and kinematic mechanisms governing colloid aggregation based on the presence or absence of pinned colloids. Supported by minimal theoretical models, we find that pinning decreases the entropic contributions to the free energy, rendering pinned sites *disfavorable* for nucleation (SM Movie S1). Thus, our work provides direct evidence that the physics of nucleation in the presence of mobility impurities in colloidal vapor deposition are primarily entropy-driven rather than those by energetic considerations.

## Vapor Deposition Experiments

The schematic of the experimental setup for colloidal vapor deposition is illustrated in Figure 1A. A suspension of monodisperse colloidal particles of diameter,  $\sigma = 1.0 \mu\text{m}$ , with size polydispersity of  $\sim 6\%$  (Supplementary Text) (21, 22), were allowed to sediment under gravity onto a glass substrate at a steady flux of  $F = (6.0 \pm 0.5) \times 10^{-5}$  monolayers/s. Prior to the start of the experiment, the glass substrate was featured with randomly distributed pinned particles by spin-coating the substrate with those used for sedimentation. This process ensured that the pinned particles matched the sedimenting ones in all aspects except for their mobility, such as shape, size, and inter-particle interactions. In all our experiments, the mean separation between pinned particles,  $L_p = (22.5 \pm 1.3)\sigma$ .

After sedimentation onto the substrate, the colloids diffuse on the surface with diffusivity,  $D$ , and eventually aggregate with neighboring colloids, either with or without a pinned particle. To minimize the desorption of sedimented colloids from the substrate, non-adsorbing depletants were added to the colloidal suspension, inducing short-range attractive forces between colloids and the substrate as well as between colloids themselves. The introduction of depletants serves another purpose in our experiments: systematically increasing the concentration of depletant particles,  $c$ , correlates with a decrease in the diffusivity of colloids on the substrate (inset to Fig. 1A). A reduction in  $D$  decreases mobility contrast between the pinned and free colloids, and thus,  $c$  could be a potential control parameter for modulating the probability of nucleation at pinned sites.

We performed experiments at six depletion concentrations,  $(0.10 \leq c \leq 0.20)$  mg/ml. In all our experiments, the mean separation between nucleating islands,  $l$ , at maximum island density was observed to be  $l \sim (4.8 \pm 1.0)\sigma$  (23). Since  $l \ll L_p$ , the possibility of nucleation at one pinned site is independent of others, and therefore, effective interaction between pinned sites can be safely ruled out. Strikingly, regardless of the value of  $c$ , pinned sites were seldom observed to be at the centre of the growing precursor clusters (Fig. 1B & SM Fig. S1), indicating thermodynamics and kinematics of the nucleation mechanism may be altered in the presence of mobility impurities.

## Thermodynamic Stability of Precursor Clusters

For nucleation to be favored at the pinned sites, the free energy difference between precursor clusters of a specific size  $n$ , comprising a pinned particle and those composed of only free particles must be less than zero, *i.e.*,  $\Delta F_{p-f}(n) = [\Delta U_{p-f}(n) - T\Delta S_{p-f}(n)] < 0$ . Here,  $\Delta U_{p-f}(n)$  and  $\Delta S_{p-f}(n)$  are the differences in the internal energy and entropy between clusters of the same size  $n$  formed with a pinned particle and without it, and  $T$  is the room temperature at which all experiments were performed. In our calculations,  $\Delta U_{p-f}(n)$  and  $\Delta S_{p-f}(n)$  are ensemble averaged over all the clusters of size,  $n$ , that appear over the total experimental duration ( $\sim 10^4$  s). Given the steady low flux rate ( $\sim 10^{-5}$  monolayer/s) and typical diffusivity of about  $6 \times 10^{-2} \sigma^2/\text{s}$  (inset to Fig. 1A), the nucleation processes at play in the individual precursor clusters can be considered to be in a quasi-static equilibrium with the local environment. While any nucleation process is inherently a non-equilibrium dynamical phenomenon, concepts from equilibrium statistical mechanics are often crucial to building their understanding (24, 25). Hence, we have employed and estimated conventional thermodynamic variables such as  $\Delta U_{p-f}(n)$  and  $\Delta S_{p-f}(n)$  from the experimental observations of the colloid dynamics to investigate any potential preferential nucleation at pinned sites.

The contributions to the internal energy of any precursor cluster are expected to be proportional to the number of bonds in the cluster due to the short-range nature of depletion-induced attractions (26). Defining  $NB(n)$  as the number of bonds in a cluster with a fixed number of colloidal particles,  $n$ , we obtain the probability distribution,  $P(NB)$ , over all the configurations of the colloids observed over the total experimental duration. We find  $P(NB)$  to be unimodal for all  $n$ , irrespective of whether a cluster contains a pinned particle or not (top left inset to Fig. 2A).

Next, using  $P(NB)$ , we find the average number of bonds,  $\langle NB(n) \rangle$ , for each  $n$  (bottom inset to Fig. 2A), and subsequently estimate  $\Delta U_{p-f}(n)$  (Fig. 2A). As expected, for a fixed  $c$ ,  $\langle NB(n) \rangle$  increases with  $n$ . For a given  $n$ ,  $\langle NB(n) \rangle$  increases with  $c$  due to increased inter-particle attraction favoring compact bond configurations. Interestingly,  $\langle NB(n) \rangle$  shows a similar trend for both clusters with a pinned particle and those without it, yielding  $\Delta U_{p-f}(n) \sim 0$  (Fig. 2A). Thus, from the perspective of internal energy, the inclusion of a pinned particle in

precursor clusters may have no discernible impact on their thermodynamic stability. Having discussed the role of internal energy, we now shift our focus to the entropic contributions to free energy.

When considering a cluster of size  $n$ , multiple unique bond connectivities are possible for a fixed  $NB$  (Fig. 2B) (27). To quantify the entropic contributions to the free energy, we need to identify, enumerate, and determine the probability of occurrence of these unique configurations. We can then determine the entropy of a cluster of size  $n$  as  $S(n) = -k_B \sum_i [p(\mu_i) \log(p(\mu_i))]$  (28), where  $p(\mu_i)$  represents the probability of the  $i^{th}$  unique microstate observed during the total experimental duration and  $k_B$  is the Boltzmann constant. In our context, we define topologically distinct coarse-grained microstates as configurations with a unique arrangement of bond connectivity (Fig. 2B). To catalog all unique coarse-grained microstates, we map all bond configurations for each  $n$  onto their respective adjacency matrices,  $A_{n \times n}$  (29). Each element  $a_{(l,m)}$  of this matrix indicates the presence (1) or absence (0) of a bond between particles  $l$  and  $m$ . Subsequently, we identify the unique isomorphic bond configurations (microstates) and obtain the probabilities  $p(\mu_i)$  for each  $\mu_i$  corresponding to a particular  $n$  (30, 31).

Unlike the internal energy, the entropy for  $n \geq 7$  exhibits a distinct profile between clusters featuring a pinned particle and those comprising only free particles (inset to Fig. 2C). Remarkably, for  $n \geq 7$  and a particular  $c$ , we find that  $\Delta S_{p-f} < 0$  (Fig. 2C), resulting in  $\Delta F_{p-f} > 0$ . Thus, clusters with a pinned particle are thermodynamically less stable than clusters of the same size comprising all free particles, suggesting that pinned particles are not the preferred centers for nucleation. Surprisingly, as evidenced by the variation of  $\Delta S_{p-f}$  with  $c$ , the entropic constraints on clusters with pinned particle increase with decreasing diffusivity of the free colloids on the substrate (Fig. 2C). In other words, the strength of depletion concentration,  $c$ , can be adjusted to tune the likelihood of nucleation at pinned sites.

Guided by experimental phenomenology, we have constructed a minimal theoretical model to capture the observed nucleation processes. Modelling colloids as hard spheres hopping on a triangular lattice, the Markov matrix can be mapped to a ferromagnetic spin-1/2 Heisenberg model (32, 33). The ground state of such a Hamiltonian, corresponding to the steady state of the Markov matrix, represents an equal probability distribution of all possible states of a fixed number of particles on the lattice, satisfying the hard sphere constraint. Pinning a particle thus cor-

responds to fixing a spin to  $+1/2$  state on the particular site in the Heisenberg lattice Hamiltonian (Supplementary Text).

By sampling typical configurations in the steady state ( $\sim 10^5$ ), we isolate the cluster distributions for a fixed cluster size  $n$ , both with and without a pinned particle. Consistent with the experimental findings, we observe no significant change in the  $P(NB)$  between clusters with a pinned particle and those comprising all free particles (top right inset to Fig. 2A, & SM Figs. S2 and S3). This indicates that the bond probability distribution is primarily governed by the configurations of lattice animals rather than being influenced by energetic considerations (34–36). Furthermore, we estimate the configurational entropy of the clusters and, again consistent with experimental findings, we find that pinning a particle in a cluster indeed reduces the entropy compared to those composed of free particles (Fig. 2C, & SM Fig. S4), making them less favorable to serve as nucleation sites. Moreover, these also make it plausible why our observations show pinned sites to either remain as single entities or predominantly located at the edge of the crystallite (Fig. 1B & SM Fig. S1).

In order to further distil the dynamical processes within the precursor clusters, we analyze small-sized clusters, both with and without a pinned particle. We attempt to identify the critical nuclei size,  $n_c$ , which marks the threshold where cluster growth becomes favorable. To estimate  $n_c$ , we track all clusters of size  $n$  and their subsequent most probable cluster size (SM Fig. S5). Interestingly, we find that for clusters formed out of all free particles,  $n_c$  can be determined for all  $c$  and were observed to be in the range  $4 \leq n_c \leq 13$ . However, in a surprising contrast, when any cluster contains a pinned particle, the analysis for  $n_c$  displays no discernible trend at any  $c$  (SM Fig. S5), indicating a significant disruption to the nucleation process due to pinning. Notably, relying solely on free energy arguments, as previously discussed, fails to elucidate this behavior, especially for cases where  $n < 7$  (and  $n_c < 7$ ) where  $\Delta F_{p-f} \sim 0$ . We, therefore, turn to investigate the rate at which individual clusters change from one configuration to another and if pinning causes any geometrical obstructions to such processes.

## Kinematics of Precursor Clusters

During the initial stages of vapor deposition, as colloids from the bulk of the suspension consistently land on the substrate to join precursor clusters, the rate at which these clusters navigate their free energy landscape dictates not only the fate of precursor clusters but also sets the stage for the stability and growth of larger crystallites. For instance, in vapor-deposited molecular glasses, faster surface diffusion facilitates the exploration of low-energy configurations, enhancing their stability (37, 38). Similarly, in our case, even when two clusters of identical size have the same entropy and, therefore, equivalent thermodynamic stability ( $n < 7$ ), their kinematics may still differ, affecting the time required to achieve more stable configurations for ensuing growth. Here, the rearrangement of particles within each cluster leads to the exploration of various microstates. Consequently, the rate at which these microstates are explored, along with the number of unique particles participating in this exploration over the cluster's lifespan, becomes crucial for stability. While the former dictates the pace of exploration across the free energy landscape, the latter ensures thoroughness in exploring this terrain.

To quantify the rate, we track the temporal evolution of clusters of size  $n$  as they transition between different microstates,  $\mu_k$ , at time intervals,  $\Delta t = 0.2$  s, for all the clusters of size  $n$  (Fig. 3A & SM Fig. S6). For each observed transition between distinct microstates over its appearance duration,  $t_k$ , a counter,  $c_k(t)$ , is incremented by unity, finally yielding,  $c_k(t = t_k) = C_k$  (Fig. 3B). We then determine rate of accessing the microstates,  $\dot{\mu}(n) = [\langle \frac{C_k}{t_k} \rangle_k]_n$ , where  $\langle \rangle_k$  represents ensemble average over all the clusters,  $k$ , of size  $n$ . Similarly, we determine the total number of unique particles,  $\mathcal{N}_k$ , that participated in the temporal evolution of  $\mu_k$  over  $t_k$ , and define the rate associated with  $\mathcal{N}_k$  as,  $\dot{\mathcal{N}}(n) = [\langle \frac{\mathcal{N}_k}{t_k} \rangle_k]_n$ . Once again, the analysis for  $\dot{\mu}(n)$  and  $\dot{\mathcal{N}}(n)$  is performed for clusters incorporating a pinned particle and for those entirely composed of free particles. Note, the necessity for clusters to persist sufficiently longer in time, precludes any such analysis for  $n > 7$ ; the range already explored through entropic arguments.

As anticipated, for a fixed  $c$ , both  $\dot{\mu}(n)$  and  $\dot{\mathcal{N}}(n)$  increases with  $n$  (Figs. 3C & D). Remarkably, while  $\Delta F_{p-f} \sim 0$  for  $n < 7$ ,  $\dot{\mu}(n)$  and  $\dot{\mathcal{N}}(n)$ , are consistently lower for clusters containing a pinned particle compared to those consisting solely of free particles (Fig. 3C and D & SM Fig. S6)). Thus, clusters with pinned particles

not only exhibit a slower traversal through their free energy landscape but also engage fewer unique particles in their exploration of the free energy landscape compared to clusters without pinned particles. This hampers the ability of clusters with pinned particles to promptly attain a stable configuration, as evidenced by the difficulty in determining  $n_c$  for clusters with a pinned particle (SM Fig. S5). Taken together, the presence of pinned particles fails to serve as preferred nucleation sites. Nonetheless, the likelihood of nucleation at the pinned sites can be controlled by tuning  $c$ .

## Spatial Extent of Vibrational Modes in Crystallites

Finally, we turn our focus to the later stages of growth to examine the dynamics of the crystallites that have formed, particularly at large monolayer coverages,  $\Theta$ . It comes as no surprise that within the crystallite, the vibrational amplitude of colloids noticeably decreases in proximity to a pinned particle (SM Fig. S7). This decrease suggests the localization of vibrational modes within the film, which we have quantified. However, given the challenges of locating crystallites with a pinned particle at their center and the presence of diffusing colloids in the second layer of the growing thin film, potentially disrupting analysis of vibrational modes, we adapted to a new experimental design (Supplementary Text). Remarkably, within an experimental area of about  $10^5 \sigma^2$ , we only encountered a tiny fraction ( $\sim 1\%$ ) of instances wherein crystallites contained a pinned particle away from their edges; the remainder were located at the periphery of the crystallite. Additionally, no growth occurred at  $\sim 15\%$  of the pinned sites, in concordance with our earlier conclusion that pinned particles do not facilitate nucleation.

To analyze the localization of the vibrational modes, we first calculate the normal modes of vibrations for two sub-regions: one with the pinned particle at the center and the other without it (Fig. 4A). This calculation, performed on the displacement covariance matrix, provides eigenvectors,  $\mathbf{e}_m$ , and eigenfrequencies,  $\omega_m$  (Supplementary Text) (39, 40). Here,  $m$  denotes the mode index. Next, we measure the participation ratio of the particles in the sub-region to each of the modes,  $[PR(\omega)]_m$ , that satisfies Debye scaling (SM Fig.S8).  $[PR(\omega)]_m = (\sum_i^N (\mathbf{e}_{m,i})^2)^2 / (2N \sum_i^N (\mathbf{e}_{m,i})^4)$ , where  $\mathbf{e}_{m,i}$  is polarization vector of  $i^{th}$ -particle in mode index,  $m$ , and  $N$  corresponds to the total number of particles in the sub-region (39). The probability distribution of the



participation ratio,  $P(PR)$ , for the sub-region with a pinned particle peaks at a smaller value of  $PR$  than those without it (Fig. 4B). Moreover, from the mean of the participation ratios,  $[\langle PR \rangle]_p < [\langle PR \rangle]_f$ , which clearly indicates that the modes in crystallites with a pinned particle are more localized compared to crystallites with all free particles. Note, however, that the mobility impurities do not disturb local structural symmetry of the crystallite and is otherwise statically indistinguishable from depositing particles. Thus our work shows that strategic incorporation of such impurities can significantly impact and can be used to engineer mechanical properties of the thin films and realize novel materials (41).

## Discussion

Our study unveils the critical influence of mobility impurities with unchanged inter-particle interaction potential on the nucleation and growth of precursor clusters in colloidal vapor deposition. Through a combination of thermodynamic and kinematic measurements, using both experiments and associated theoretical insights, we demonstrate that pinned colloids fail to serve as preferred sites for nucleation. Importantly, the nucleation probability at pinned sites can be further modulated by manipulating the mobility of free colloids on the substrate. Moreover, in later stages of growth, pinned sites induce localization of vibrational modes in the thin film, potentially altering its mechanical stability (41). These findings collectively highlight the role of mobility impurities as a novel platform for influencing nucleation mechanisms in the initial stages of growth processes in vapor deposition techniques. While our investigation focused on single pinned particles with short-range attractions, it would be worthwhile to delve into scenarios involving long-range interactions, directional bonding, and the implications of pinning larger crystallites, which may be relevant to self-assembly in molecular systems (14, 15, 41).

## References

1. L. Granasy, *et al.*, *Nat. Mater.* **2**, 92 (2003).
2. S. Esch, M. Hohage, T. Michely, G. Comsa, *Phys. Rev. Lett.* **72**, 518 (1994).
3. I. Musevic, M. Skarabot, U. Tkalec, M. Ravnik, S. Zumer, *Science* **313**, 954 (2006).

4. W. Zhong, Y. Cai, D. Tomanek, *Nature* **362**, 435 (1993).
5. G. Duscher, M. F. Chisholm, U. Alber, M. Rühle, *Nat. Mater.* **3**, 621 (2004).
6. J. R. Kermode, *et al.*, *Nat. Commun.* **4**, 2441 (2013).
7. T. Delattre, *et al.*, *Nat. Phys.* **5**, 208 (2009).
8. D. Mocatta, *et al.*, *Science* **332**, 77 (2011).
9. A. Cacciuto, S. Auer, D. Frenkel, *Nature* **428**, 404 (2004).
10. A. Navrotsky, *Proc. Natl. Acad. Sci. USA* **101**, 12096 (2004).
11. S. Elhadj, J. De Yoreo, J. Hoyer, P. Dove, *Proc. Natl. Acad. Sci. USA* **103**, 19237 (2006).
12. V. W. De Villeneuve, *et al.*, *Science* **309**, 1231 (2005).
13. E. Allahyarov, K. Sandomirski, S. U. Egelhaaf, H. Löwen, *Nat. Commun.* **6**, 7110 (2015).
14. L. Ma, *et al.*, *J. Am. Chem. Soc.* **143**, 13314 (2021).
15. Y.-L. Hong, *et al.*, *Science* **369**, 670 (2020).
16. W. Ma, J. F. Lutsko, J. D. Rimer, P. G. Vekilov, *Nature* **577**, 497 (2020).
17. S. Liu, L. Bönig, J. Detch, H. Metiu, *Phys. Rev. Lett.* **74**, 4495 (1995).
18. H. Kakoty, R. Banerjee, C. Dasgupta, A. Ghosh, *Phys. Rev. Lett.* **117**, 258002 (2016).
19. G. Kellogg, *Phys. Rev. Lett.* **72**, 1662 (1994).
20. S. van Teeffelen, C. N. Likos, H. Löwen, *Phys. Rev. Lett.* **100**, 108302 (2008).
21. W. Stöber, A. Fink, E. Bohn, *J. Colloid Interface Sci.* **26**, 62 (1968).
22. L. Zhang, *et al.*, *Langmuir* **25**, 2711 (2009).

23. R. Ganapathy, M. R. Buckley, S. J. Gerbode, I. Cohen, *Science* **327**, 445 (2010).
24. U. W. Pohl, *Epitaxy of semiconductors: physics and fabrication of heterostructures* (Springer Nature, 2020).
25. I. V. Markov, *Crystal growth for beginners: fundamentals of nucleation, crystal growth and epitaxy* (World Scientific, 2016).
26. G. Meng, N. Arkus, M. P. Brenner, V. N. Manoharan, *Science* **327**, 560 (2010).
27. R. W. Perry, M. C. Holmes-Cerfon, M. P. Brenner, V. N. Manoharan, *Phys. Rev. Lett.* **114**, 228301 (2015).
28. C.-e. A. Chang, W. Chen, M. K. Gilson, *Proc. Natl. Acad. Sci. USA* **104**, 1534 (2007).
29. F. Pietrucci, W. Andreoni, *Phys. Rev. Lett.* **107**, 085504 (2011).
30. A. Jüttner, P. Madarasi, *Discrete Appl. Math.* **242**, 69 (2018).
31. L. P. Cordella, P. Foggia, C. Sansone, M. Vento, *3rd IAPR-TC15 workshop on graph-based representations in pattern recognition* (Citeseer, 2001), pp. 149–159.
32. W. Feller, *An introduction to probability theory and its applications, Volume I* (John Wiley & Sons, 1968).
33. R. Livi, P. Politi, *Nonequilibrium Statistical Physics: A Modern Perspective* (Cambridge University Press, 2017).
34. J. W. Essam, *Reports on Progress in Physics* **43**, 833 (1980).
35. D. Stauffer, A. Aharony, *Introduction to percolation theory* (Taylor & Francis, 2018).
36. M. F. Sykes, M. Glen, *Journal of Physics A: Mathematical and General* **9**, 87 (1976).
37. S. F. Swallen, *et al.*, *Science* **315**, 353 (2007).
38. L. Zhu, *et al.*, *Phys. Rev. Lett.* **106**, 256103 (2011).
39. K. Chen, *et al.*, *Phys. Rev. Lett.* **105**, 025501 (2010).

40. J. Melio, S. E. Henkes, D. J. Kraft, *Phys. Rev. Lett.* **132**, 078202 (2024).
41. X. Gu, Y. Wei, X. Yin, B. Li, R. Yang, *Rev. Mod. Phys.* **90**, 041002 (2018).

## Acknowledgements

Authors thank Mahesh M Bandi, Sriram Ramaswamy, Chandan Dasgupta, John C. Crocker, Samudrajit Thapa, Prasanna Venkatesh B., K. Hima Nagamanasa, Anirban Sain, Pinaki Majumdar and Sankalp Nambiar for useful comments and discussions. The idea for this project originated from preliminary experimental observations made by C.K.M. during his PhD studies in the Ganapathy Group at JNCASR. We acknowledge Rajesh Ganapathy for his comments on this problem. **Funding:** We gratefully acknowledge financial support from the Department of Science and Technology (Government of India), INSPIRE fellowship IF200274 (N.H.B.), Prime Minister Research Fellowship (S.M.), IIT Kanpur Initiation Grant through IITK/PHY/2022010 (A.A.), IIT Gandhinagar through IP/IITGN/PHY/CM/2021/11 (C.K.M.) and the Start-up Research Grant of Science and Engineering Research Board of Government of India through SRG/2021/001077 (C.K.M.). **Competing interests:** The authors declare no competing interest. **Data and materials availability:** The microscopy videos and datasets generated during analyses in the current study are large ( $> 2$  terabytes) and hence are not publicly available, but can be made available from the corresponding author on request.

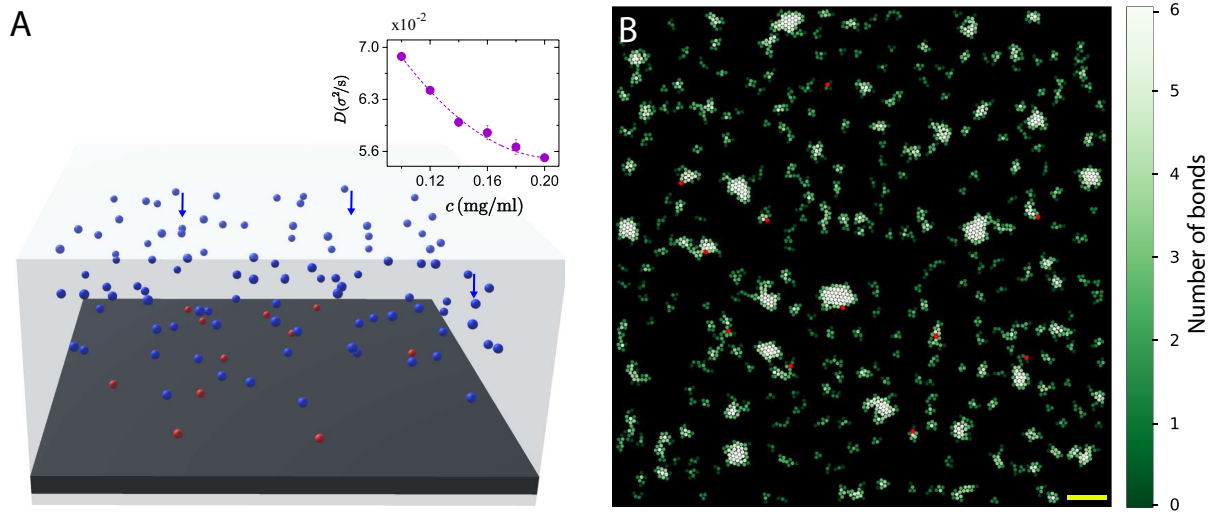
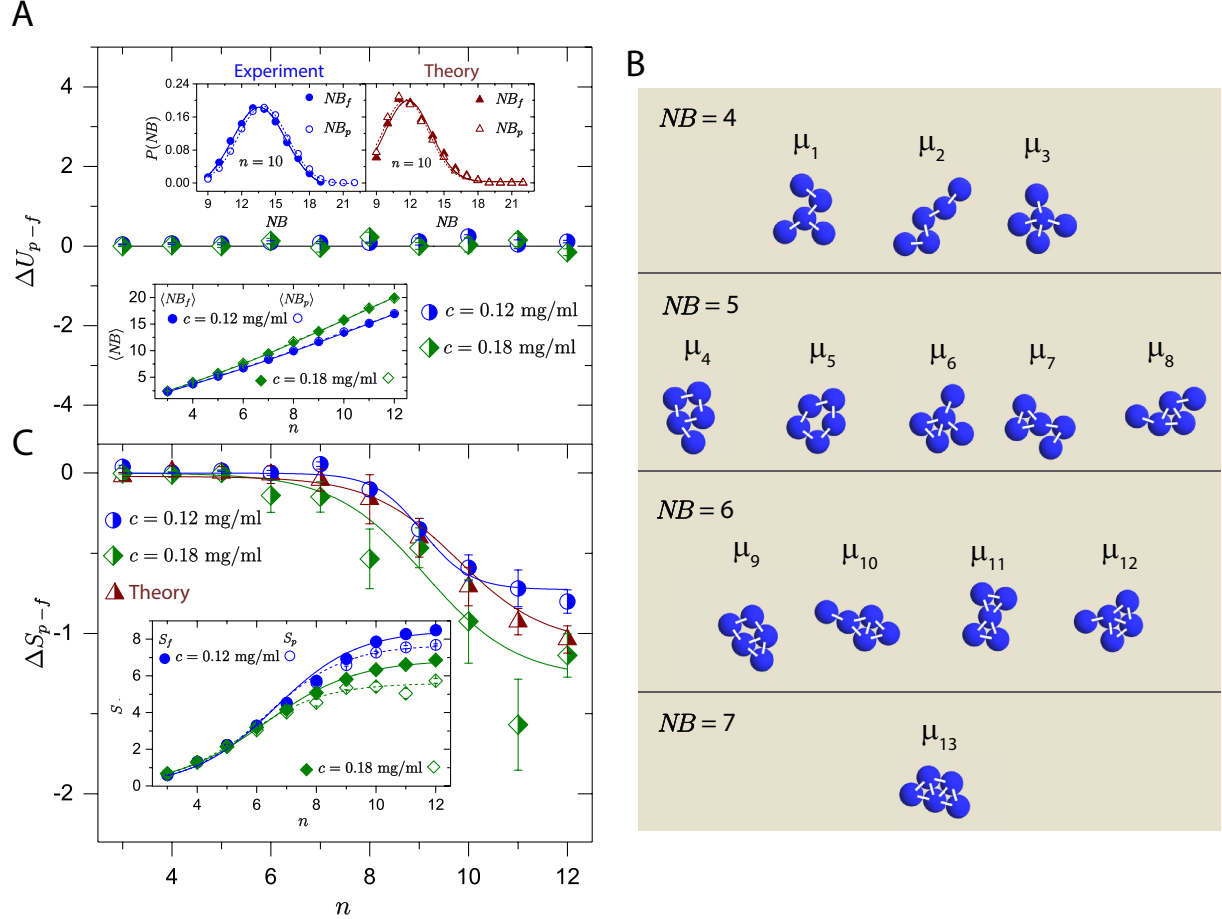
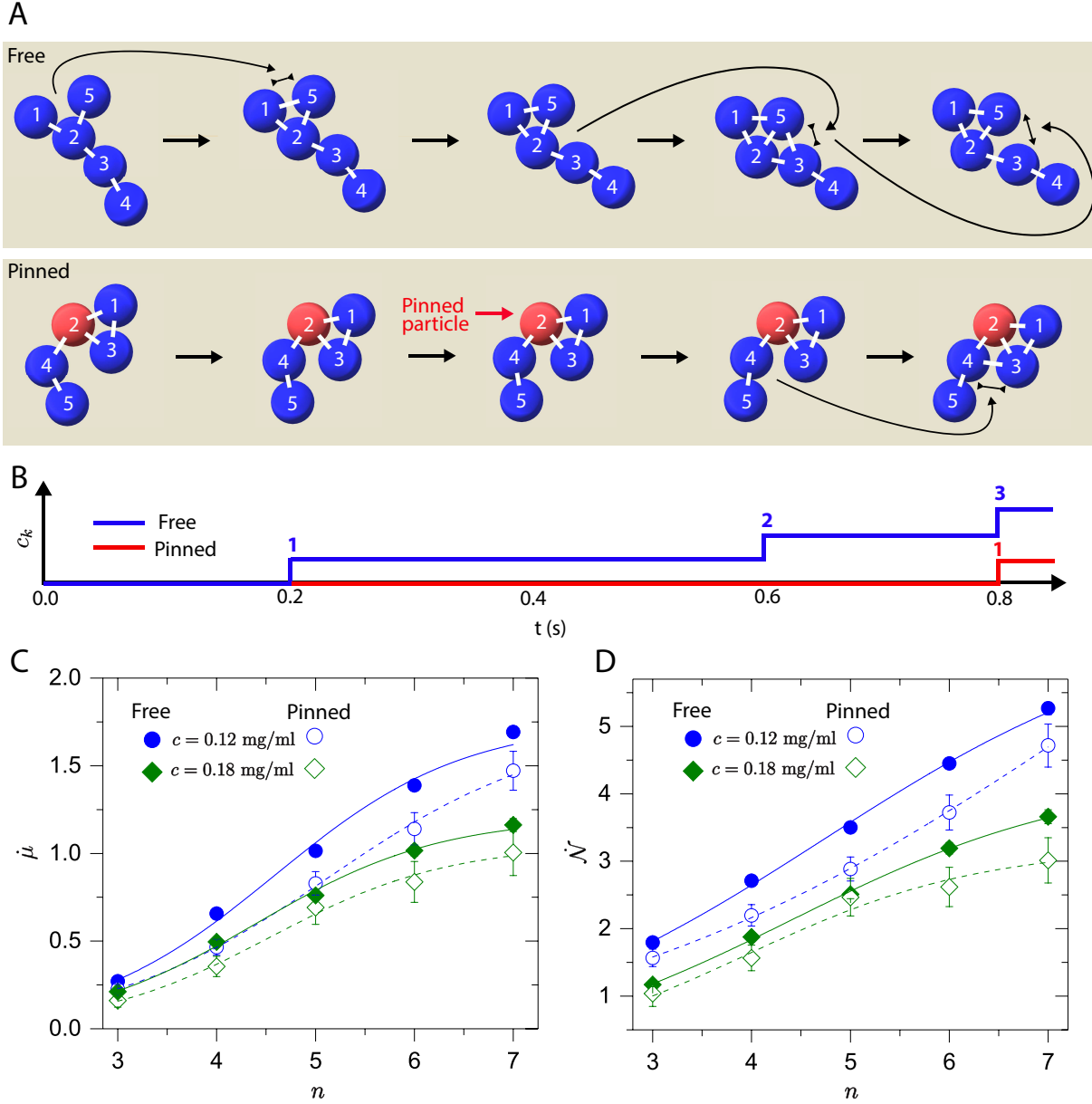


Figure 1: **Experimental setup and characterization** (A) Schematic of the experimental set-up showing pinned colloidal particles in red and the sedimenting ones in blue. Inset shows the surface diffusivity of single colloids,  $D$  (in the units of  $\sigma^2/s$ ), versus  $c$ . The dashed curve is a guide to the eye. (B) Snapshot of the field-of-view at monolayer coverage,  $\Theta = 0.20$ , at  $c = 0.12$  mg/ml. The particles have been color-coded based on the number of bonds they form in their nearest-neighbor shell. Pinned particles are shown in red. The scale bar denotes  $10 \mu\text{m}$ .



**Figure 2: Internal energy and entropy of precursor clusters.** (A)  $\Delta U_{p-f}(n)$  in the units of scaled  $k_B T$  versus cluster size,  $n$ , at different  $c$ . The top panel inset shows  $P(NB)$  for  $n = 10$ -particle clusters with one pinned particle (open symbols) and all of them mobile (solid symbols) from experiment at  $c = 0.12$  mg/ml (left panel) and theory (right panel). The bottom inset shows the average number of bonds,  $\langle NB(n) \rangle$ , versus  $n$  for clusters with a pinned particle (open symbols) and with all free particles (solid symbols). (B) Enumeration of experimentally observed topologically distinct coarse-grained microstates,  $\{\mu_i\}$ , for cluster size,  $n = 5$ , with unique arrangements of bond connectivity for different total number of bonds,  $NB$ . (C)  $\Delta S_{p-f}(n)$  in the units of  $k_B$  versus  $n$  for the same  $c$  as in (A) and theoretical model (brown). The inset shows the entropy of clusters as a function of  $n$  for clusters with a pinned particle (open symbols) and with all free particles (solid symbols). For theoretical curves in (A) and (C), cluster distributions are obtained from steady-state configurations of a Markov matrix governing hard spheres hopping on a triangular lattice of 256 sites. About  $10^5$  configurations are taken for each of the particle densities between 0.1 and 0.6 in intervals of 0.01, and for the pinning case, 1% of sites are kept immobilized. Solid and dashed curves in (A) and (C) are guides to the eye.



**Figure 3: Kinematics of precursor clusters.** (A) Rendering from the experiment at  $c = 0.12$  mg/ml to illustrate the change in microstate for a given 5-particle cluster comprising of all free particles (top panel) and with one pinned particle (bottom panel) at  $\Delta t = 0.2$  s. (B) Counter,  $c_k$ , tracking microstate transitions in a cluster with all free particles (blue line) and with one pinned particle (red line) for the temporal evolution of clusters shown in (A). (C)  $\dot{\mu}_n$  and (D)  $\dot{\mathcal{N}}(n)$  versus  $n$  for clusters (persisting for at least 0.5 s) with one pinned particle (open symbols) and with all free particles (solid symbols) at different  $c$ . Solid and dashed curves in (C) and (D) are guides to the eye.

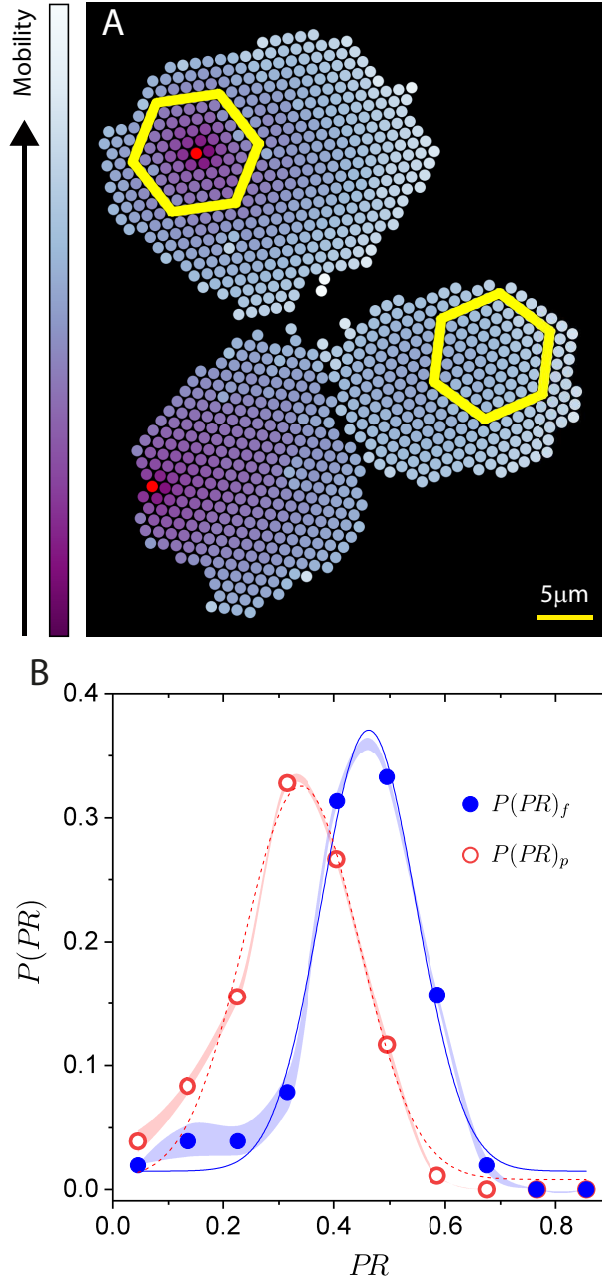


Figure 4: **Localization of normal modes of vibrations.** (A) Snapshot of crystallites at  $c = 0.12$  mg/ml showing sub-regions (yellow hexagon) utilized for analysis of localization of normal modes of vibrations. Free particles are color-coded based on their mobility, and pinned particles are rendered in red. The particle's mobility is calculated as the square root of the standard deviation of the particle's position, determined for and consequently averaged over all non-overlapping one-second slices of data. (B) Probability distribution of the participation ratio  $PR$  for the sub-regions with a pinned particle (open symbol) and with all the free particles (solid symbols). The respective standard errors obtained from two different experiments with similar sub-regions, as shown in (A), are shown using ribbons. The dashed (red) and solid (blue) curves are Gaussian fits to the data.